RESEARCH ARTICLE

National Science Review
8: nwaa187, 2021
https://doi.org/10.1093/nsr/nwaa187
Advance access publication 24 August 2020

MATERIALS SCIENCE

Tracking structural evolution: *operando* regenerative CeO_x/Bi interface structure for high-performance CO_2 electroreduction

Ruichao Pang[1,2,†], Pengfei Tian[1,†], Hongliang Jiang[1,*], Minghui Zhu[1], Xiaozhi Su[3], Yu Wang[3], Xiaoling Yang[2], Yihua Zhu[2], Li Song[4] and Chunzhong Li[1,2,*]

[1]Key Laboratory for Ultrafine Materials of Ministry of Education, School of Chemical Engineering, East China University of Science and Technology, Shanghai 200237, China; [2]Shanghai Engineering Research Center of Hierarchical Nanomaterials, School of Materials Science and Engineering, East China University of Science and Technology, Shanghai 200237, China; [3]Shanghai Institute of Applied Physics, Chinese Academy of Sciences, Shanghai 201204, China and [4]National Synchrotron Radiation Laboratory, University of Science and Technology of China, Hefei 230029, China

***Corresponding authors.** E-mails: jhlworld@ecust.edu.cn; czli@ecust.edu.cn
†Equally contributed to this work.

Received 11 May 2020; **Revised** 22 July 2020; **Accepted** 18 August 2020

ABSTRACT

Unveiling the structural evolution and working mechanism of catalysts under realistic operating conditions is crucial for the design of efficient electrocatalysts for CO_2 electroreduction, yet remains highly challenging. Here, by virtue of *operando* structural measurements at multiscale levels, it is identified under CO_2 electroreduction conditions that an as-prepared CeO_2/BiOCl precatalyst gradually evolves into CeO_x/Bi interface structure with enriched Ce^{3+} species, which serves as the real catalytically active phase. The derived CeO_x/Bi interface structure compared to pure Bi counterpart delivers substantially enhanced performance with a formate Faradaic efficiency approaching 90% for 24 hours in a wide potential window. The formate Faradaic efficiency can be further increased by using isotope D_2O instead of H_2O. Density functional theory calculations suggest that the regenerative CeO_x/Bi interfacial sites can not only promote water activation to increase local $^*H$ species for CO_2 protonation appropriately, but also stabilize the key intermediate $^*OCHO$ in formate pathway.

Keywords: CO_2 electroreduction, electrocatalyst, nanosheet, structural evolution, interface

INTRODUCTION

Recent years have witnessed explosive development in electrochemical CO_2 reduction into valuable chemicals or fuels [1–5]. CO_2 electroreduction is considered as a promising route to utilizing renewable electricity [6,7]. Designing high-performance electrocatalysts is pivotal to tuning CO_2 activation, thus achieving the highly selective CO_2 conversion into target products [8–10]. However, the rational design of electrocatalysts faces severe challenges, because most of the catalysts would go through dynamic structural evolution under applied electric field [1,6,11–13]. The ambiguous evolution rules also hinder the uncovering of the working mechanism. Generally, the real catalytically active phase is inconsistent with the as-prepared or post-catalyzed catalyst structure. The established structure–performance relationship based on *ex situ* static characterizations does not match the realistic catalytic phenomenon. For instance, positive-valence metal species would be electrochemically transformed into so-called zero-valent metals during CO_2 electroreduction [6,7,14]. In this regard, some studies pointed out that the presence of slight positive-valence metal species in the derived structure is the key to realizing highly efficient CO_2 electrocatalysis [15–17]. More importantly, the evolution processes are closely related to the precatalytic structure and electrocatalytic conditions, including potentials, electrolytes, temperature, etc [11,12]. Nevertheless, it is not clear how the catalyst structure evolves, and how a real catalytically active component catalyzes CO_2 conversion under the corresponding environmental conditions [18]. To tackle the problems, *in situ*/*operando* characterization techniques, such as *operando* Raman and X-ray absorption fine structure (XAFS) measurements, are solid methods to track

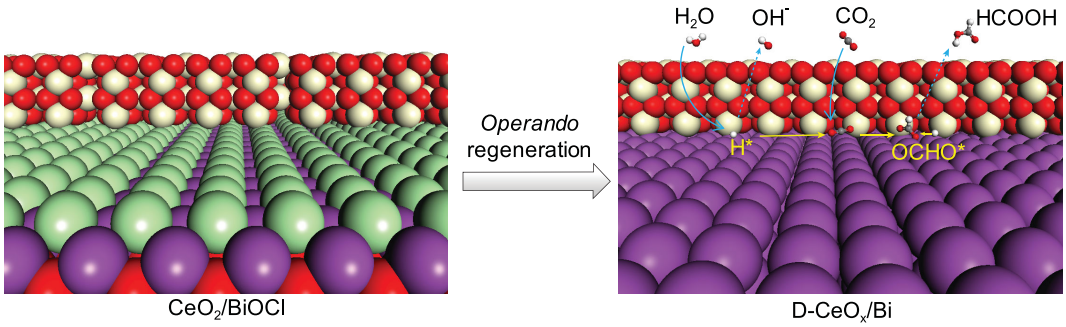

Figure 1. Schematic illustration of the *operando* regeneration of CeO_2/BiOCl into D-CeO_x/Bi during CO_2 electroreduction. Purple, green, yellow, gray, red and white spheres are Bi, Cl, Ce, C, O and H atoms, respectively.

structural change, identify real active phases and uncover the underlying mechanism, thus guiding the structure design of highly active and robust catalysts [19–22].

Herein, we *operando* probed the structural evolution of as-prepared BiOCl nanosheets loaded with CeO_2 (denoted as CeO_2/BiOCl), which was obviously different from *ex situ* static characterizations either before or after a reaction. It has been found that the CeO_2/BiOCl precatalyst gradually evolved into a stable CeO_x/Bi interface structure with increased Ce^{3+} species, under cathodic reduction potential with a certain strength (Fig. 1). The structural regeneration was attributed to the irreversible reduction processes of Bi^{3+} and Ce^{4+} cations. Especially, the presence of CeO_2 component could facilitate the regeneration process, as evidenced by *operando* Raman results. The derived CeO_x/Bi interface structure (named as D-CeO_x/Bi) enabled highly selective and stable CO_2 electroreduction to formate, significantly outperforming the Bi and CeO_x (denoted as D-Bi and D-CeO_x) counterparts derived from cathodic reduction of BiOCl and CeO_2. D_2O isotope labeling experiments have also been performed to probe the working mechanism, verifying that hydrogen source of formate product originated from water activation. Based on the *operando* structural identifications, the structure model for the regenerated Bi/CeO_x interface structure was established. The computed Gibbs free energies of the reaction species indicated that the formation of key intermediate *OCHO for formate pathway could be boosted at the regenerative CeO_x/Bi interfacial sites, thereby rationalizing the high selectivity experimentally.

RESULTS AND DISCUSSION

The BiOCl and CeO_2/BiOCl were obtained via a propylene oxide-assisted hydrolytic process, followed by thermal treatment at 400°C in air (see details in Methods). X-ray diffraction (XRD) measurements clarified that both BiOCl and CeO_2 components existed in the CeO_2/BiOCl (Supplementary Fig. 1). The CeO_2 nanoparticles (NP) were loaded onto typical BiOCl nanosheets to form interfacial structure, as confirmed by transmission electron microscopy (TEM) and corresponding fast Fourier Transform images (Fig. 2a and b, Supplementary Figs 2–4). Subjected to a cathodic reduction at −1.0 V versus reversible hydrogen electrode (RHE) for 30 minutes in CO_2-saturated 0.5 M $KHCO_3$ solution, slight structure change was observed for the D-CeO_x/Bi (Fig. 2c), probably due to the irreversible reduction of Bi^{3+} and Ce^{4+} cations [6,7,14]. The NP-loaded interfacial structure was maintained (Fig. 2d). As shown in Supplementary Fig. 5, the lattice spacing of 0.33 and 0.27 nm in the D-CeO_x/Bi were attributed to the Bi (012) and CeO_2 (110) planes (JCPDS No. 44-1246: Bi; JCPDS No. 34-0394: CeO_2), respectively [6,23,24]. The results indicated that the BiOCl was converted into metallic Bi, and the CeO_2 was apparently unchanged. We also identified that the two phases kept close interfacial contact from high angle annular dark field scanning TEM (HAADF-STEM) and the corresponding energy-dispersive X-ray (EDX) elemental mapping (Fig. 2e). Furthermore, the transformation process was also evidenced by X-ray photoelectron spectroscopy (XPS) results. The peaks of 164.8 and 159.5 eV corresponding to Bi^{3+} species disappeared (Fig. 2f), and two new peaks at 163.9 and 158.6 eV ascribed to metallic Bi^0 were detected after the reduction process [14]. The Ce species kept typical signal peaks corresponding to Ce^{3+} and Ce^{4+} species both before and after the reduction (Fig. 2g). It is noted that the Ce^{3+} species were obviously enriched from 26.1% to 42.3% as a result of the increase of oxygen defects during the reduction process (Supplementary Table 1) [24]. And these oxygen defects were readily filled by the hydroxyl in aqueous solution [25]. *Ex situ* Raman measurements were also performed to characterize the D-CeO_x/Bi.

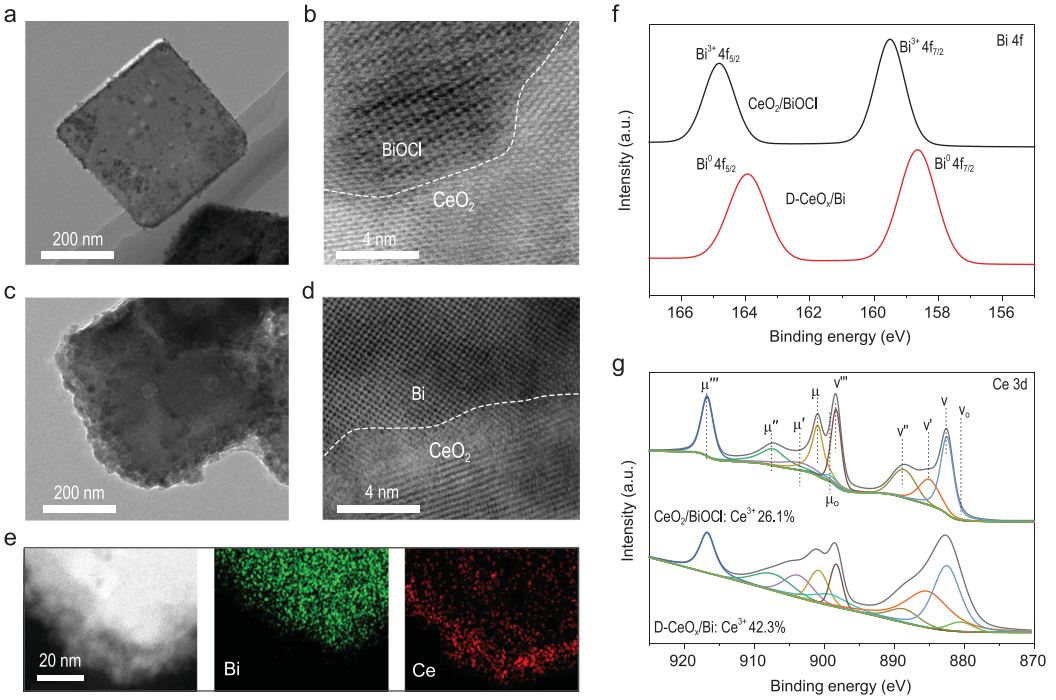

Figure 2. *Ex situ* static characterizations before and after the reaction. (a) TEM and (b) HRTEM images of the CeO_2/BiOCl. (c) TEM image, (d) HRTEM image and (e) the corresponding EDX elemental mapping of the D-CeO_x/Bi. (f) Bi 4f and (g) Ce 3d XPS spectra of the CeO_2/BiOCl and D-CeO_x/Bi.

As shown in Supplementary Fig. 6, for the CeO_x sample, the peak at 1168 cm^{-1} corresponded to the second-order longitudinal optical (2LO) mode of fluorite phase [26]. As to D-CeO_x/Bi, the peaks at 75 and 103 cm^{-1} corresponded to typical vibration signal of metallic Bi [27]. Compared to that of CeO_x sample, a new peak at 1071 cm^{-1} emerged for the D-CeO_x/Bi, which was ascribed to the formation of Bi-O-Ce bonds [28,29]. The Raman results also indicated that Bi^{3+} of BiOCl was reduced to Bi^0 species, and Bi/CeO_x interfaces existed in the D-CeO_x/Bi. The standard electrode potential of E^0 (Bi^{3+}/Bi^0) is 0.308 V versus RHE [30], much more positive than the cathodic reduction potential of −1.0 V versus RHE. Therefore, the BiOCl was readily converted into metallic Bi. The E^0 (Ce^{3+}/Ce^0) is −2.336 V versus RHE, and E^0 (CeO_2/Ce^{3+}) is 1.4 V versus RHE. Thus Ce^{4+} species in the CeO_2 component were readily reduced to the Ce^{3+} species, but were hardly converted to Ce^0 species. It has to be pointed out that nanostructured metallic Bi is air-sensitive, and is easily surface-oxidized [24]. And the CeO_2 has the high ability to capture and release oxygen [31,32]. Therefore, combined with the above *ex situ* static characterizations, *in situ*/*operando* structural measurements have to be employed to identify the real active components accurately.

We carried out *operando* characterization measurements at multiscale levels to track the structural evolution and obtain dynamic structural information of the catalysts in CO_2-saturated 0.5 M $KHCO_3$ solution. First *operando* XRD measurement was performed to identify the evolution of crystal structure. Typically, from the *operando* XRD patterns (Supplementary Fig. 7), it can be seen that the peak of about $2\theta = 25.9^\circ$ corresponded to the (101) plane of BiOCl. When the cathodic reduction potential was increased to −0.9 V versus RHE, the peak disappeared. The new peak at about $2\theta = 27.2^\circ$ corresponding to the (012) plane of metallic Bi was emerged. The peak at about $2\theta = 26.6^\circ$ ascribed to carbon paper nearly remained unchanged. The signal from CeO_2 component was not detected in the *operando* test condition due to the relatively low content. The transformation of crystal structure was in accordance with the above TEM results. To achieve the identification of the dynamic geometric structure, we performed potential- and time-dependent *operando* Raman spectra (Fig. 3, Supplementary Figs 8 and 9). At open circuit potential (OCP), four typical Raman peaks at 67, 151, 207 and 405 cm^{-1} were presented (Fig. 3), which were assigned to the A_{1g} external Bi-Cl stretching mode, the A_{1g} internal Bi-Cl stretching mode, the E_g external Bi-Cl stretching mode and the external Bi-O stretching vibration in the BiOCl structure, respectively [33,34]. The peak at 461 cm^{-1} corresponded to the F_{2g} mode of Ce-O-Ce symmetric stretching

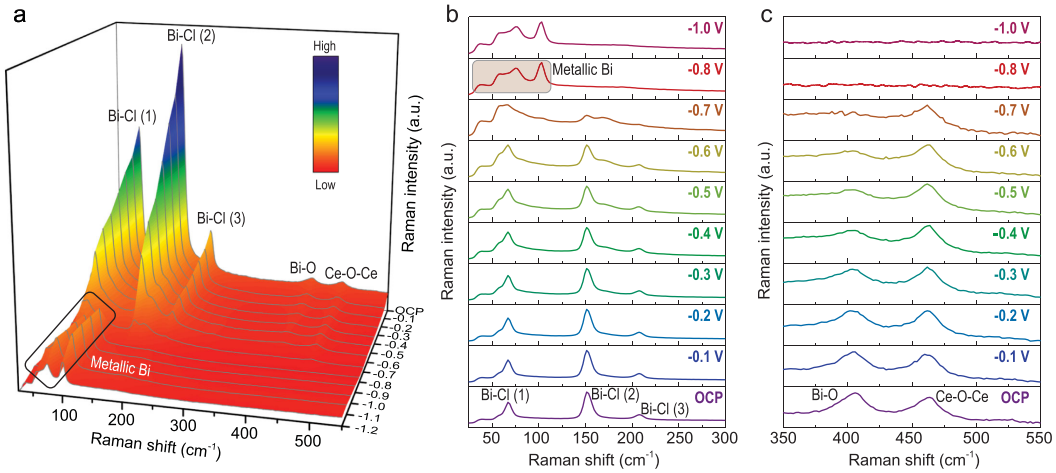

Figure 3. *Operando* Raman characterizations towards regeneration process. (a) Potential-dependent *operando* Raman spectra of the CeO_2/BiOCl. Potential-dependent *operando* Raman spectra of the CeO_2/BiOCl at wavenumber region of 25 to 300 cm^{-1} (b) and 350 to 550 cm^{-1} (c), respectively.

vibration in the CeO_2 structure [35]. With gradually increasing cathodic potential to −0.7 V versus RHE, the peaks ascribed to that of the BiOCl were in decline (Fig. 3a and b). Meanwhile, it was accompanied by two new characteristic peaks at 75 and 103 cm^{-1}, which were corresponding to typical vibration signal of metallic Bi [27]. Also note that the peak ascribed to the F_{2g} mode of Ce-O-Ce symmetric stretching vibration also remained almost unchanged until −0.7 V (Fig. 3c). The peak vanished at higher potentials. With the increase of oxygen defects and reduced Ce^{3+} ions at higher potentials, the signature vibrational band would exhibit a reduced and widened model system [26,36], thus leading to the apparent disappearance of the peak at about 461 cm^{-1}. Furthermore, we also dissected *operando* Raman spectra from 950 to 1200 cm^{-1} (Supplementary Fig. 8). The peak of about 1071 cm^{-1} remained nearly unchanged under applied potential windows, manifesting in the persistence of the Bi/CeO_x interface throughout electrochemical tests. Additionally, by analyzing time-dependent *operando* Raman spectra at −0.9 V versus RHE (Supplementary Fig. 9), it was also found that the CeO_2/BiOCl compared to the BiOCl exhibited faster transformation process, probably because the presence of the CeO_2 could facilitate water dissociation to increase local proton concentration for the BiOCl reduction [37]. To further gain the information for electronic properties, we employed *operando* X-ray absorption near edge structure (XANES) measurements. From the normalized XANES spectra and local enlargement at the Bi L_3-edge (Supplementary Fig. 10), it was found that the BiOCl subjected to the cathodic reduction current of 1 and 10 mA/cm^2 aligned well with the Bi foil, and the shift of absorption edge could not be observed, demonstrating the complete absence of positive-valence Bi species [6,14]. The normalized Ce L_3-edge XANES spectra (Supplementary Fig. 11) show that the Ce species of CeO_2/BiOCl was almost reduced to Ce^{3+} under CO_2 electroreduction conditions [35]. The result is inconsistent with Ce 3d XPS results as a result of the high ability of oxygen capture for oxygen vacancy-rich CeO_x in air [31,32]. These *operando* characterization results provided solid evidences for the structural regeneration of the as-prepared CeO_2/BiOCl precatalyst into the defect-enriched CeO_x/Bi interface structure under the actual CO_2 electroreduction condition.

The electrochemical performance was estimated in a two-compartment gas-tight H-type cell within 0.5 M $KHCO_3$ solution (see details in Methods). In order to accomplish the structural regeneration, first the as-prepared CeO_2/BiOCl and BiOCl loaded onto carbon paper were electrochemically treated for 30 minutes at −0.9 V versus RHE. The linear sweep voltammetry (LSV) curves (Supplementary Fig. 12) displayed that the current densities were remarkably increased in CO_2-saturated electrolyte in contrast to Ar-saturated electrolyte, indicating that both the D-CeO_x/Bi and D-Bi favored CO_2 reduction over hydrogen evolution reaction (HER). Through analyses of the products, the D-CeO_x/Bi with Bi/Ce ratio (3 : 1) exhibited the optimized performance, displaying the highest formate Faradaic efficiency ($FE_{formate}$) of 92.0% at −0.9 V versus RHE (Fig. 4a, Supplementary Figs 13 and 14). The corresponding formate partial current density reached 22.1 mA/cm^2 (Fig. 4b), which was nearly two times higher than that of the D-Bi (12.0 mA/cm^2). The electrocatalytic performance

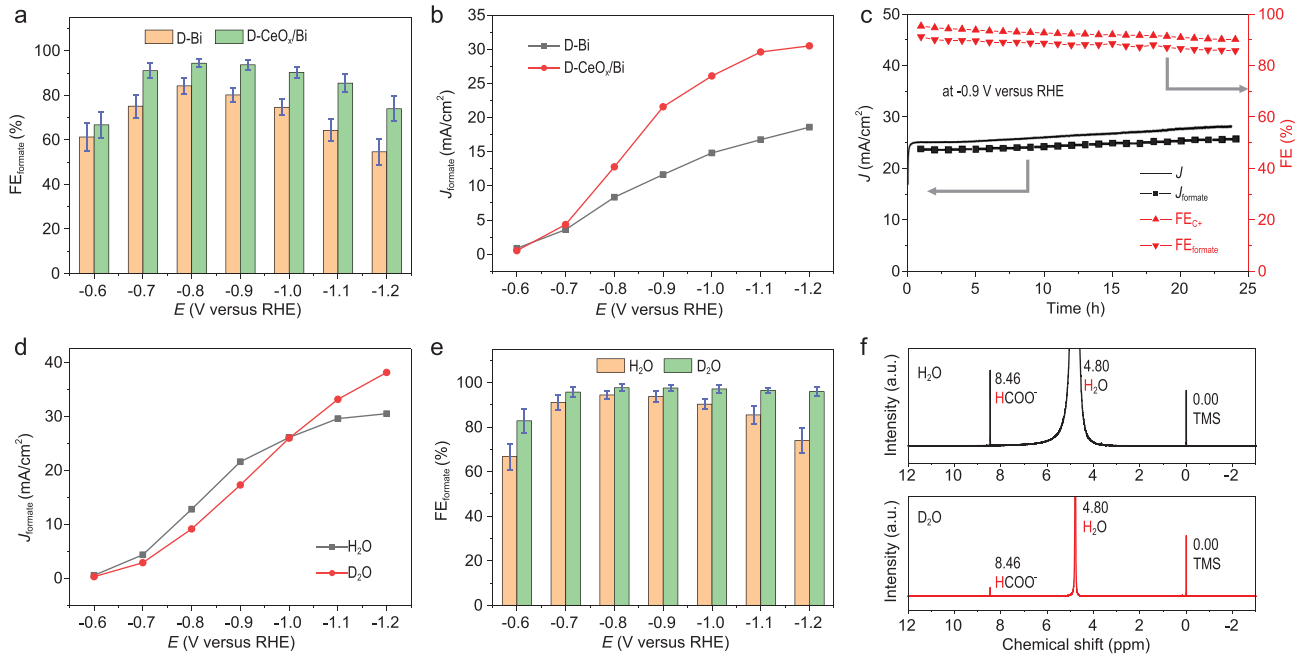

Figure 4. Performance evaluation of CO_2 electroreduction. (a) Potential-dependent $FE_{formate}$ of the D-Bi and D-CeO_x/Bi. (b) Potential-dependent formate partial current density of the D-Bi and D-CeO_x/Bi. (c) Long-term stability and selectivity of D-CeO_x/Bi at −0.9 V versus RHE. (d) Potential-dependent formate partial current density of the D-CeO_x/Bi under H_2O and D_2O conditions. (e) Potential-dependent $FE_{formate}$ of the D-CeO_x/Bi under H_2O and D_2O conditions. (f) ^1H nuclear magnetic resonance (NMR) spectra of the D-CeO_x/Bi under H_2O and D_2O conditions.

of both D-Bi and D-CeO_x/Bi is significantly better than of D-CeO_x (Supplementary Fig. 15), evidencing the importance of Bi components on high formate selectivity [6,7,14]. The electrochemical surface area (ECSA)-normalized partial current density of D-CeO_x/Bi was still 1.5 times larger than that of D-Bi (Supplementary Fig. 16), suggesting the key role of the interfacial structure on enhancing intrinsic activity [25,35]. We also identified that the FE of products that contain carbon element (formate and CO) maintained over 90% at a wide potential window of approximately −0.7 to −1.0 V (Supplementary Fig. 17). In addition to the good activity and selectivity, the D-CeO_x/Bi also displayed long-term stability of formate production for 24 hours (Fig. 4c).

To probe the underlying mechanism of CO_2 electroreduction into formate onto the D-CeO_x/Bi, we carried out *operando* Fourier transformation infrared (FTIR) measurements and D_2O labeling experiments. As shown in Supplementary Fig. 18a, the broad band between 1350 and 1450 cm^{-1} arose from the dissolved CO_3^{2-}/HCO_3^- and formate [38–40]. The broad band gradually rose with increasing reduction potential, suggesting the accumulation of formate [38]. The reversed peak at about 1650 cm^{-1} is attributed to the consumption of interfacial H_2O [41,42], implying the H_2O participation in the formate formation. Meanwhile, the doublet peak at about 2350 cm^{-1} declined when the cathodic reduction potential or the electrolytic time was increased (Supplementary Fig. 18b and c), which are attributed to the consumption of gaseous CO_2 [43]. From potential-dependent current densities of the D-CeO_x/Bi under H_2O and D_2O conditions (Fig. 4d, Supplementary Fig. 19), we could identify that the partial current densities of total formate ($HCOO^-$ and $DCOO^-$) under D_2O condition were lower than that under H_2O condition when the potential was between −0.6 and −1.0 V. For the potential window of −1.0 to −1.2 V, the partial current densities under D_2O condition were larger relative to that under H_2O condition. The $FE_{formate}$ under D_2O condition was always higher than that under H_2O condition under total measured potential window (Fig. 4e, Supplementary Fig. 20). The changed activity and selectivity meant that the formate formation was moderately promoted, and the hydrogen evolution was inhibited under D_2O condition. To disclose the reason, the $HCOO^-$ content in the total electrolyte was determined by ^1H nuclear magnetic resonance (NMR) (Fig. 4f). Through analyzing the relative amount of $HCOO^-$ and $DCOO^-$ in the total formate (see details in Methods), it was uncovered that the $DCOO^-$ content of 91.7% at −0.9 V was much greater than the $HCOO^-$ content, which demonstrated that the hydrogen source of formate

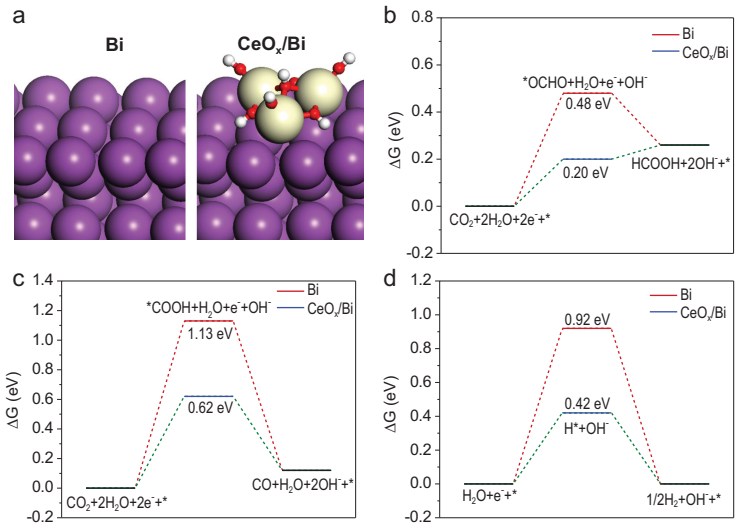

Figure 5. Theoretical calculations for the Bi and CeO_x/Bi. (a) Optimized structure models for the Bi and CeO_x/Bi. Purple, yellow, red and white spheres are Bi, Ce, O, and H atoms, respectively. (b, c) Gibbs free energy diagrams for CO_2RR to HCOOH and CO onto the Bi and CeO_x/Bi structure models, respectively. (d) Gibbs free energy diagrams for H_2O activation onto the Bi and CeO_x/Bi structure models.

mainly came from water activation [44]. Therefore, it could be easily understood that the water activation under D_2O condition was harder than that under H_2O condition, causing the insufficient supply of absorbed *D species for the formate formation at low overpotentials. At high overpotentials, the supply of the absorbed *D species was sufficient. The appropriately inhibited water activation enabled less release of gaseous hydrogen, thus leading to the higher formate partial current densities and selectivity.

We further employed density functional theory (DFT) calculations to understand the enhanced reason of the regenerated Ce^{3+}-enriched CeO_x/Bi interface toward formate formation. Based on the above *operando* structural identifications, structure models for the Bi and CeO_x/Bi surfaces as well as corresponding adsorption configurations of intermediates were rationally established (Fig. 5a and Supplementary Fig. 21). In the structure models, the Ce^{3+} species were considered as the Ce atoms that were bound with hydroxyls [25]. The formation of *OCHO and *COOH intermediate were demonstrated as the key of HCOOH and CO pathway, respectively [45,46]. For the HCOOH pathway, the Gibbs free energies for the formation of *OCHO onto Bi and CeO_x/Bi surfaces were 0.48 and 0.20 eV, respectively (Fig. 5b). The introduction of CeO_2 onto Bi surface efficiently stabilized the *OCHO through binding one O atom of *OCHO with the Ce atom (Supplementary Fig. 21c). On the other hand, the calculated Gibbs free energies for CO pathway onto both the Bi and CeO_x/Bi surfaces were larger than that for HCOOH pathway (Fig. 5c), strongly supporting higher selectivity toward formate than that toward CO onto typical Bi-based materials. To understand the effect of CeO_x/Bi interface on water activation, we also calculated the Gibbs free energies of HER onto Bi and CeO_x/Bi surfaces (Fig. 5d). The Gibbs free energies for the *H formation onto the Bi surface were 0.92 eV. The value for the CeO_x/Bi surface was remarkably decreased to 0.42 eV. The results indicated that water activation could be efficiently enhanced through introducing CeO_2 components onto the Bi surface. In terms of the competition between HER and HCOOH formation, it could be identified that the formation energies of the key intermediate *OCHO were always lower than that of *H, theoretically interpreting the preferential HCOOH formation onto the CeO_x/Bi interfacial structure, despite the boosted water activation. Combining these calculation results with the above isotope labeling evidences, it could be reasonably deduced that the water activation at the interfacial sites was properly improved to provide the *H species for the formation of the key intermediate *OCHO in HCOOH pathway, thus accounting for the increased selectivity of formate experimentally.

CONCLUSION

In summary, we have reported the tracking of the dynamic structural evolution of as-prepared CeO_2/BiOCl precatalyst under realistic CO_2 electroreduction conditions, by combining *operando* XRD, Raman and XAFS measurements. It has comprehensively been demonstrated that the real active catalyst for CO_2 reduction is regenerative CeO_x/Bi interface structure with increased Ce^{3+} species. High Faradaic efficiency and stability for formate formation are finally exhibited onto the derived CeO_x/Bi interface structure. D_2O isotope labeling results have verified that the hydrogen elements of formate product originate from water activation. We have revealed that the regenerative CeO_x/Bi interfacial sites can properly promote water activation to supply hydrogen source for the formate formation, and lower the energy barrier of the CO_2 protonation into the key intermediate *OCHO. This work provides insights into structural evolution and activity origin of catalysts under realistic working conditions, and highlights the importance of mechanism study and catalyst design based *operando* feedback information.

METHODS

Synthesis of CeO_2/BiOCl and BiOCl

CeO_2/BiOCl was synthesized through a propylene oxide (PO)-assisted hydrolytic process. Typically,

$BiCl_3$ (1.5 mmol) and $CeCl_3{\cdot}7H_2O$ (0.5 mmol) were firstly dissolved in deionized water (4.5 ml). Then PO (1.3 ml) was added in the above liquid to obtain the liquid emulsion. The solution was stirred for 6 hours and then aged for 6 hours. The obtained precipitate was collected by centrifuging and washed five times with deionized water and ethanol, then dried at 60°C for 8 hours in the air. Finally the obtained product was placed into a muffle furnace and heated to 400°C for 2 hours at a rate of 3°C/min. BiOCl counterpart was prepared with the similar method except that $CeCl_3{\cdot}7H_2O$ was not added.

Electrochemical measurements

Electrochemical measurements were performed in a three-electrode two-compartment cell separated by Nafion 117 membrane in an electrochemical workstation (CHI 660E). ^{1}H NMR spectroscopy was used to analyze liquid products. The ^{1}H NMR spectra were recorded on an Ascend 600-MHz Unity plus spectrometer (Bruker). The electrolyte (0.5 mL) was mixed with deuterated water (0.1 mL), using 1% tetramethylsilane (TMS) as internal standard. CO_2RR measurements in D_2O solution were carried out with similar processes to that in H_2O. The total amount of formate ($HCOO^-$ and $DCOO^-$) in electrolytes was quantified by High Performance Liquid Chromatography (HPLC). ^{1}H NMR was used to determine the amount of $HCOO^-$ product. The concentration of formate was quantitatively determined from its NMR peak area relative to the internal standard by using the calibration curve for standard HCOOK solutions (Supplementary Fig. 22). *Operando* XRD experiments were performed using an X-Ray Polycrystalline Diffractometer (Bruker AXS D8 Advance). *Operando* Raman measurements were conducted in a LabRAM HR800 confocal microscope (Horiba Jobin Yvon). *Operando* XAFS measurements were performed in Shanghai Synchrotron Radiation Facility (BL14W1, SSRF), China. The *operando* FTIR experiments were performed with Perkin Elmer Spectrum 100 FT-IR spectrometer equipped with diamond attenuated total reflection (UATR) accessory and a mercury cadmium telluride (MCT) detector. More electrochemical and *operando* measurement details were given in the supplementary information.

DFT calculation

DFT calculations were performed using the Vienna ab-initio simulation package (VASP) [47,48]. Considering that the CO_2RR was carried out at aqueous phase condition, a fully hydroxylated ceria cluster ($Ce_3O_7H_7$) supported on Bi(110) surface is adopted to simulate the D-CeO_x/Bi catalyst, denoted as $Ce_3O_7H_7$/Bi(110) [49]. Bi(110) surface was adopted to model the Bi catalyst for reference. Bi(110) substrate was established as a four-layered slab with (3×3) unit cells, of which the bottom two layers were fixed. The top two layers of Bi(110), the $Ce_3O_7H_7$ cluster and the surface species were fully relaxed. A vacuum spacing of 12 Å along the normal direction (z) to the surface and a $1 \times 2 \times 1$ Gamma centered k-point sampling were used for the models. More computational details were given in the supplementary information.

SUPPLEMENTARY DATA

Supplementary data are available at *NSR* online.

ACKNOWLEDGEMENTS

The authors thank Shanghai Synchrotron Radiation Facility (BL14W1, SSRF).

FUNDING

This work was supported by the National Natural Science Foundation of China (21838003, 91834301 and 21978278), the Shanghai Scientific and Technological Innovation Project (18JC1410500 and 19JC1410400) and the Fundamental Research Funds for the Central Universities (222201718002).

AUTHOR CONTRIBUTIONS

C.Z.L. and H.L.J. planned the project and designed the experiments. R.C.P. carried out most of the sample preparation and material measurements. P.F.T. performed DFT calculations and analyzed the data. X.Z.S. and Y.W. conducted *operando* XAS test. X.L.Y. and Y.H.Z. contributed to the STEM analysis. L.S. helped to conduct XAS analysis. M.H.Z. helped to analyze *operando* Raman and FTIR data. R.C.P., P.F.T., H.L.J. and C.Z.L. co-wrote the paper. All authors discussed the results and commented on this manuscript.

Conflict of interest statement. None declared.

REFERENCES

1. Wu Y, Jiang Z and Lu X *et al.* Domino electroreduction of CO_2 to methanol on a molecular catalyst. *Nature* 2019; **575**: 639–42.
2. Zhang L, Zhao Z and Wang T *et al.* Nano-designed semiconductors for electro- and photoelectro-catalytic conversion of carbon dioxide. *Chem Soc Rev* 2018; **47**: 5423–43.
3. Su X, Yang X-F and Huang Y *et al.* Single-atom catalysis toward efficient CO_2 conversion to CO and formate products. *Acc Chem Res* 2019; **52**: 656–64.

4. Ren W and Zhao C. Paths towards enhanced electrochemical CO_2 reduction. *Natl Sci Rev* 2020; **7**: 7–9.
5. Han N, Wang Y and Ma L *et al.* Supported cobalt polyphthalocyanine for high-performance electrocatalytic CO_2 reduction. *Chem* 2017; **3**: 652–64.
6. Gong Q, Ding P and Xu M *et al.* Structural defects on converted bismuth oxide nanotubes enable highly active electrocatalysis of carbon dioxide reduction. *Nat Commun* 2019; **10**: 2807.
7. Han N, Wang Y and Yang H *et al.* Ultrathin bismuth nanosheets from *in situ* topotactic transformation for selective electrocatalytic CO_2 reduction to formate. *Nat Commun* 2018; **9**: 1320.
8. Ma W, Xie S and Liu T *et al.* Electrocatalytic reduction of CO_2 to ethylene and ethanol through hydrogen-assisted C-C coupling over fluorine-modified copper. *Nat Catal* 2020, **3**: 478–87.
9. Liu M, Liu M and Wang X *et al.* Quantum-dot-derived catalysts for CO_2 reduction reaction. *Joule* 2019; **3**: 1703–18.
10. Liu M, Pang Y and Zhang B *et al.* Enhanced electrocatalytic CO_2 reduction via field-induced reagent concentration. *Nature* 2016; **537**: 382–6.
11. Jiang H, He Q and Li X *et al.* Tracking structural self-reconstruction and identifying true active sites toward cobalt oxychloride precatalyst of oxygen evolution reaction. *Adv Mater* 2019; **31**: 1805127.
12. Jiang H, Lin Y and Chen B *et al.* Ternary interfacial superstructure enabling extraordinary hydrogen evolution electrocatalysis. *Mater Today* 2018; **21**: 602–10.
13. Liang Y, Zhou W and Shi Y *et al.* Unveiling *in situ* evolved In/In_2O_{3-x} heterostructure as the active phase of In_2O_3 toward efficient electroreduction of CO_2 to formate. *Sci Bull* 2020; **65**: 1547–54.
14. He S, Ni F and Ji Y *et al.* The p-orbital delocalization of main-group metals to boost CO_2 electroreduction. *Angew Chem Int Ed* 2018; **57**: 16114–9.
15. Chen Y and Kanan MW. Tin oxide dependence of the CO_2 reduction efficiency on tin electrodes and enhanced activity for tin/tin oxide thin-film catalysts. *J Am Chem Soc* 2012; **134**: 1986–9.
16. De Luna P, Quintero-Bermudez R and Dinh C-T *et al.* Catalyst electro-redeposition controls morphology and oxidation state for selective carbon dioxide reduction. *Nat Catal* 2018; **1**: 103–10.
17. Lei Q, Zhu H and Song K *et al.* Investigating the origin of enhanced C_{2+} selectivity in oxide-/hydroxide-derived copper electrodes during CO_2 electroreduction. *J Am Chem Soc* 2020; **142**: 4213–22.
18. Deng P, Wang H and Qi R *et al.* Bismuth oxides with enhanced bismuth-oxygen structure for efficient electrochemical reduction of carbon dioxide to formate. *ACS Catal* 2020; **10**: 743–50.
19. Ye K, Zhou Z and Shao J *et al. In situ* reconstruction of a hierarchical $Sn\text{-}Cu/SnO_x$ core/shell catalyst for high-performance CO_2 electroreduction. *Angew Chem Int Ed* 2020; **59**: 4814–21.
20. Zhu Y, Wang J and Chu H *et al. In situ*/*operando* studies for designing next-generation electrocatalysts. *ACS Energy Lett* 2020; **5**: 1281–91.
21. Jiang H, He Q and Zhang Y *et al.* Structural self-reconstruction of catalysts in electrocatalysis. *Acc Chem Res* 2018; **51**: 2968–77.
22. Wang Y, Zhou W and Jia R *et al.* Unveiling the activity origin of a copper-based electrocatalyst for selective nitrate reduction to ammonia. *Angew Chem Int Ed* 2020; **59**: 5350–4.
23. Zhang S, Xia Z and Zou Y *et al.* Interfacial frustrated Lewis pairs of CeO_2 activate CO_2 for selective tandem transformation of olefins and CO_2 into cyclic carbonates. *J Am Chem Soc* 2019; **141**: 11353–7.
24. Lin Y, Yang L and Jiang H *et al.* Sulfur atomically doped bismuth nanobelt driven by electrochemical self-reconstruction for boosted electrocatalysis. *J Phys Chem Lett* 2020; **11**: 1746–52.
25. Dong H, Zhang L and Li L *et al.* Abundant Ce^{3+} ions in $Au\text{-}CeO_x$ nanosheets to enhance CO_2 electroreduction performance. *Small* 2019; **15**: 1900289.
26. Lin B, Liu Y and Heng L *et al.* Morphology effect of ceria on the catalytic performances of Ru/CeO_2 catalysts for ammonia synthesis. *Ind Eng Chem Res* 2018; **57**: 9127–35.
27. Zhang W, Hu Y and Ma L *et al.* Liquid-phase exfoliated ultrathin Bi nanosheets: uncovering the origins of enhanced electrocatalytic CO_2 reduction on two-dimensional metal nanostructure. *Nano Energy* 2018; **53**: 808–16.
28. Satsuma A, Yanagihara M and Ohyama J *et al.* Oxidation of CO over Ru/Ceria prepared by self-dispersion of Ru metal powder into nano-sized particle. *Catal Today* 2013; **201**: 62–7.
29. Huang W and Gao Y. Morphology-dependent surface chemistry and catalysis of CeO_2 nanocrystals. *Catal Sci Technol* 2014; **4**: 3772–84.
30. Lide DR. *CRC Handbook of Chemistry and Physics*, 87th edn. Boca Raton: CRC Press/Taylor and Francis Group, 2006.
31. Hu Q, Huang B and Li Y *et al.* Methanol gas detection of electrospun CeO_2 nanofibers by regulating Ce^{3+}/Ce^{4+} mole ratio via Pd doping. *Sens Actuators B Chem* 2020; **307**: 127638.
32. Michel CR and Martínez-Preciado AH. CO sensor based on thick films of 3D hierarchical CeO_2 architectures. *Sens Actuators B Chem* 2014; **197**: 177–84.
33. Davies JED. Solid state vibrational spectroscopy-III[1] The infrared and raman spectra of the bismuth(III) oxide halides. *J Inorg Nucl Chem* 1973; **35**: 1531–4.
34. Lei Y, Wang G and Song S *et al.* Synthesis, characterization and assembly of BiOCl nanostructure and their photocatalytic properties. *CrystEngComm* 2009; **11**: 1857–62.
35. Lee CW, Shin S-J and Jung H *et al.* Metal-oxide interfaces for selective electrochemical C-C coupling reactions. *ACS Energy Lett* 2019; **4**: 2241–8.
36. Schilling C, Hofmann A and Hess C *et al.* Raman spectra of polycrystalline CeO_2: a density functional theory study. *J Phys Chem C* 2017; **121**: 20834–49.
37. Liu Z, Huang E and Orozco I *et al.* Water-promoted interfacial pathways in methane oxidation to methanol on a $CeO_2\text{-}Cu_2O$ catalyst. *Science* 2020; **368**: 513–7.
38. Gao D, Zhou H and Cai F *et al.* Switchable CO_2 electroreduction via engineering active phases of Pd nanoparticles. *Nano Res* 2017; **10**: 2181–91.
39. Yang Y-Y, Ren J and Zhang H-X *et al.* Infrared spectroelectrochemical study of dissociation and oxidation of methanol at a palladium electrode in alkaline solution. *Langmuir* 2013; **29**: 1709–16.
40. Miyake H, Okada T and Samjeské G *et al.* Formic acid electrooxidation on Pd in acidic solutions studied by surface-enhanced infrared absorption spectroscopy. *Phys Chem Chem Phys* 2008; **10**: 3662–9.
41. Jiang K, Xu K and Zou S *et al.* B-Doped Pd catalyst: boosting room-temperature hydrogen production from formic acid-formate solutions. *J Am Chem Soc* 2014; **136**: 4861–4.
42. Zhang H-X, Wang S-H and Jiang K *et al. In situ* spectroscopic investigation of CO accumulation and poisoning on Pd black surfaces in concentrated HCOOH. *J Power Sources* 2012; **199**: 165–9.
43. Yuan T, Hu Z and Zhao Y *et al.* Two-dimensional amorphous SnO_x from liquid metal: mass production, phase transfer, and electrocatalytic CO_2 reduction toward formic acid. *Nano Lett* 2020; **20**: 2916–22.
44. Ma W, Xie S and Zhang X-G *et al.* Promoting electrocatalytic CO_2 reduction to formate via sulfur-boosting water activation on indium surfaces. *Nat Commun* 2019; **10**: 892.
45. Kortlever R, Shen J and Schouten KJP *et al.* Catalysts and reaction pathways for the electrochemical reduction of carbon dioxide. *J Phys Chem Lett* 2015; **6**: 4073–82.

46. Yoo JS, Christensen R and Vegge T *et al*. Theoretical insight into the trends that guide the electrochemical reduction of carbon dioxide to formic acid. *ChemSusChem* 2016; **9**: 358–63.
47. Kresse G and Furthmüller J. Efficient iterative schemes for total-energy calculations using a plane-wave basis set. *Phys Rev B* 1996; **54**: 11169–86.
48. Kresse G and Furthmüller J. Efficiency of ab-initio total energy calculations for metals and semiconductors using a plane-wave basis set. *Comput Mater Sci* 1996; **6**: 15–50.
49. Gao D, Zhang Y and Zhou Z *et al*. Enhancing CO_2 electroreduction with the metal-oxide interface. *J Am Chem Soc* 2017; **139**: 5652–5.